A coupled approach for the modelling of arc welding processes

Christel Pequet, Patrice Lasne, Makhlouf Hamide, Elisabeth Massoni, Michel Bellet

Proc. MCWASP XI, 11th Int. Conf. on Modeling of Casting, Welding and Advanced Solidification Processes, Opio, France, May 28 - June 3, 2006, C.A. Gandin, M. Bellet (eds.), The Minerals, Metals & Materials Society, Warrendale, Pennsylvania, USA (2006) 855-862

A COUPLED APPROACH FOR THE MODELLING OF ARC WELDING PROCESSES

Christel Pequet[1], Patrice Lasne[1], Makhlouf Hamide[2], Elisabeth Massoni[2], Michel Bellet[2]

[1]Transvalor SA, Parc de haute de technologie, Sophia Antipolis, 694 avenue du Dr. Donat, 06255 Mougins Cedex, France ; email : projects@transvalor.com
[2]Ecole des Mines de Paris, CEMEF, UMR CNRS 7635, BP 207, 06904 Sophia Antipolis Cedex, France ; email : michel.bellet@ensmp.fr

Keywords: welding, finite elements, thermal-metallurgical-mechanical coupling, material deposit

Abstract

A 3D finite element model is presented, addressing some major phenomena arising in arc welding as well as their interaction: heat input, metal deposit, solidification, phase transformations in the solid state and material behavior. As a result of a simulation, the shape of the weld bead, the phase distribution, residual stresses and distortions are obtained. Some application and validation cases are discussed.

Introduction

The arc welding process allows assembling parts with or without material deposit. The high temperatures reached induce structural transformations in the metal such as solid-liquid or metallurgical solid state phase changes. Deformations in the assembly and residual stresses are also generated during the welding process. All these phenomena are complex and vary according to the process parameters (type of welding process, heat source power, welding velocity, clamping, number of pass, etc). The material behavior varies during welding due to the temperature evolution and phase transformations.
Numerical simulation may help in the design and the optimization of welded assemblies. The first objectives of the simulation must be:

- To predict the geometry of the welded assembly, including weld bead shape.
- To follow the thermal and mechanical evolutions in the weld bead and in the part as well as the structural transformations and to evaluate the risks of defects during the process and in the final assembly.
- To predict the final mechanical properties of the assembly, starting from the prediction of residual stresses and structural variables.

Despite an abundant literature on welding numerical simulation (one can refer to the review of Runesson et al [1]), there is still a real challenge in the numerical modeling of welding processes, because of the diversity of the phenomena involved at different time and length scales. This paper presents a contribution in that direction, coupling thermal, mechanical and metallurgical resolutions in a 3D finite element code. An original method to simulate the metal deposit will be also described.

Metallurgical Model

During the welding operation, very high heating rate and cooling rate are obtained in the heat-affected zone of the parts and in the weld bead. This temperature evolution may induce

transformations of the initial phases of the steel in austenite during heating, then in martensite, bainite, ferrite and pearlite during cooling. The austenizing in the part during heating is partial or total. The volume fraction of austenite g_{aust} is a function of the maximum temperature reached and of the heating rate. The austenizing may be described with the following equation:

$$\frac{\partial g_{aust}}{\partial t} = (1 - g_{aust})\alpha(T - A_{c3})^{\beta} \quad (1)$$

With this simple model, the partial austenizing at temperatures lower than austenizing temperature A_{c3} is neglected and the austenizing rate is assumed to increase with temperature.
The simulation of the metallurgical transformation during cooling is based on TTT diagrams [2, 3], as illustrated in Figure 1. The incubation of ferrite, pearlite and bainite, is represented using Scheil parameter. For the growth, a Johnson-Mehl Avrami law [4] is used to compute the fraction of ferrite, pearlite or bainite transformed. The use of the TTT diagram in the case of a non-isothermal transformation is done considering its decomposition into successive isothermal transformations. An additivity principle and the notion of fictitious time are used [5].

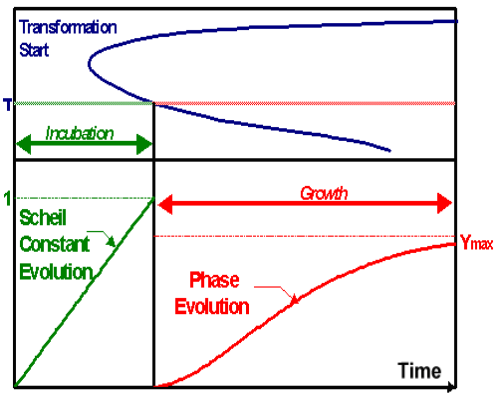

Incubation and growth in the case of an isothermal transformation

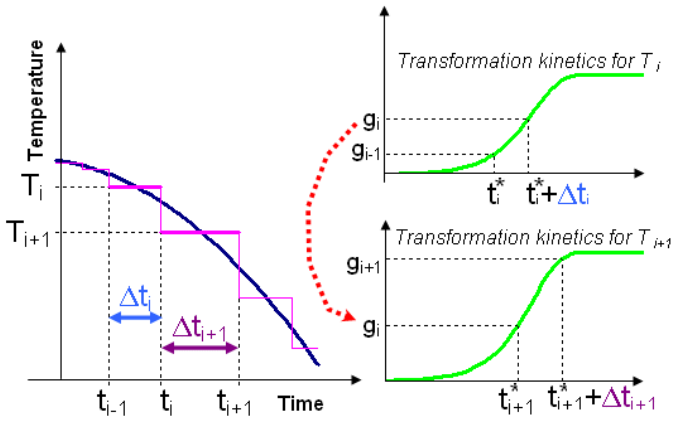

Principle of the simulation of a non-isothermal transformation

Figure 1. TTT approach (temperature, time, transformations) for modeling solid state transformations.

The martensitic transformation is predicted using the Koistinen-Marburger law [6]. The martensite volume fraction g_{mart} is a function of the temperature when the temperature is lower than the martensite transformation temperature M_s.

$$g_{mart} = g_{aust}\left(1 - e^{-A_M(M_S - T)}\right) \quad (2)$$

The metallurgical transformation is coupled with the thermal computation through the transformation enthalpy of each phase change (see next section).
The variation of density between the different phases induces volume changes during allotropic transformations. The transformation plasticity is also taken into account to represent the abnormal deformation created during the metallurgical transformation under stress [7]. In this case, the decomposition of the strain rate tensor is generalized with the following equation:

$$\dot{\boldsymbol{\varepsilon}} = [\dot{\boldsymbol{\varepsilon}}^e + \dot{\boldsymbol{\varepsilon}}^p + \dot{\boldsymbol{\varepsilon}}^{th}] + [\dot{\boldsymbol{\varepsilon}}^{tp} + \dot{\boldsymbol{\varepsilon}}^{tr}] \quad (3)$$

in which appear different contributions: $\dot{\boldsymbol{\varepsilon}}^e$ for the elastic deformation, $\dot{\boldsymbol{\varepsilon}}^p$ for the deviatoric plastic deformation and $\dot{\boldsymbol{\varepsilon}}^{th}$ for the volumetric thermal expansion, plus the contributions associated with solid state phase changes: $\dot{\boldsymbol{\varepsilon}}^{tp}$ for the deviatoric plastic transformation and $\dot{\boldsymbol{\varepsilon}}^{tr}$ for the volumetric change.

Coupling Between Metallurgical and Thermal Resolutions

As expressed above, metallurgical transformations highly depend on temperature history. Conversely, the impact of phase transformations (liquid-solid and solid-solid) on heat transfer should be considered. Applying the spatial averaging method on an elementary representative volume (REV) of the multiphase material, we get [8]:

$$\frac{\partial}{\partial t}\left(g_k \rho_k h_k\right) + \nabla \cdot \left(g_k \rho_k h_k \boldsymbol{v}_k\right) + \nabla \cdot \left\langle \boldsymbol{q}^k \right\rangle = Q_k \tag{4}$$

where k denotes either the liquid ($k = l$) or one of the possible solid phases ($k = 1, N$), h the specific enthalpy, g the volume fraction and ρ the density. Assuming the temperature uniform in the REV, neglecting advection effects and phase density differences, it yields:

$$\langle \rho \rangle \left(\sum_{i=1,N} \frac{\partial g_i}{\partial t} h_i + \frac{\partial g_l}{\partial t} h_l \right) + \langle \rho \rangle \langle c_p \rangle \frac{\partial T}{\partial t} - \nabla \cdot (\langle \lambda \rangle \nabla T) = 0 \tag{5}$$

Denoting $k = 1$ the primary solid phase, and noticing that $g_l + g_1 + \sum_{i=2,N} g_i = 1$,we get:

$$\langle \rho \rangle \langle c_p \rangle \frac{\partial T}{\partial t} + \langle \rho \rangle \frac{\partial g_l}{\partial t}(h_l - h_1) - \nabla \cdot (\langle \lambda \rangle \nabla T) = -\langle \rho \rangle \sum_{i=2,N} \frac{\partial g_i}{\partial t} h_i + \langle \rho \rangle \sum_{i=2,N} \frac{\partial g_i}{\partial t} h_1 \tag{6}$$

Denoting now $L = h_l - h_1$ the latent heat of solidification, and $\widetilde{h}(T) = \int_{T_0}^{T} \langle c_p \rangle (\tau)\, \mathrm{d}\tau + g_l L$, the final form of the conservation equation is very similar to the one that would be used for an enthalpy resolution with a unique solid phase, but it includes an additional right hand side:

$$\langle \rho \rangle \frac{\partial \widetilde{h}}{\partial t} + \nabla \cdot (\langle \lambda \rangle \nabla T) = -\langle \rho \rangle \sum_{i=2,N} \frac{\partial g_i}{\partial t} h_i + \langle \rho \rangle \sum_{i=2,N} \frac{\partial g_i}{\partial t} h_1 \tag{7}$$

This right hand side term is a source term composed of the enthalpy changes that are associated with each solid state phase change (*i-j*). It can be noticed that after solidification of the REV, we have $\sum_{i=1,N} g_i = 1$. The previous equation becomes then:

$$\langle \rho \rangle \frac{\partial \widetilde{h}}{\partial t} + \nabla \cdot (\langle \lambda \rangle \nabla T) = -\langle \rho \rangle \sum_{i=1,N} \frac{\partial g_i}{\partial t} h_i \tag{8}$$

Regarding implementation, a weak form of this equation is discretized with finite elements. The non linear resolution provides the nodal values of $\widetilde{h}$. From these values, the unknown nodal values of variables T and g_l can be calculated by solving a linear or non linear scalar equation (depending on the case: liquid, mushy, solid). This formulation permits then to take into account the energy changes associated with the solid state phase changes, while taking advantage of the stability and robustness of the enthalpy formulation for the liquid-solid phase change.

Coupling Between Metallurgical and Mechanical Resolutions

In the framework of a velocity-pressure formulation, the weak form of the momentum and mass conservation equations can be expressed as follows:

$$\begin{cases} \forall \boldsymbol{v}^* \quad \int\limits_{\Omega} \boldsymbol{s}(\boldsymbol{v}) : \dot{\boldsymbol{\varepsilon}}^* \, \mathrm{d}V - \int\limits_{\Omega} p \nabla \cdot \boldsymbol{v}^* \, \mathrm{d}V - \int\limits_{\partial\Omega} \boldsymbol{T} \cdot \boldsymbol{v}^* \, \mathrm{d}S - \int\limits_{\Omega} \rho \boldsymbol{g} \cdot \boldsymbol{v}^* \, \mathrm{d}V + \int\limits_{\Omega} \rho \frac{\mathrm{d}\boldsymbol{v}}{\mathrm{d}t} \cdot \boldsymbol{v}^* \, \mathrm{d}V = 0 \\ \forall p^* \quad \int\limits_{\Omega} p^* \, \mathrm{tr}\, \dot{\boldsymbol{\varepsilon}}^{vp} \, \mathrm{d}V = 0 \end{cases} \tag{9}$$

where $\boldsymbol{s}$ is the stress deviator, p the pressure, ρ the density, $\boldsymbol{g}$ the gravity, $\boldsymbol{v}$ the velocity field and $\boldsymbol{T}$ the external stress vector. The constitutive equations used in solidification problems have been presented in previous papers [9, 10]. Here it is just reminded that in the liquid and mushy states, steels are modeled as Newtonian and non Newtonian fluids, respectively, using a temperature dependent viscoplastic model. In the solid state they are modeled using a temperature dependent elastic-viscoplastic model. After spatial discretization using finite elements and time discretization, this results in a set of non linear equations $\boldsymbol{R}_{mech}(\boldsymbol{V},\boldsymbol{P})=0$, the unknowns of which are the velocity components and the pressure value at each node of the finite element mesh.
While the influence of stress state on solid state phase changes has not been taken into account in this work, the reverse coupling has been treated as follows. In the context of a multiphasic solid, the variables $\boldsymbol{s}$ and p have been homogenized in a very simple way, as a first approach: the velocity field is supposed identical in the different phases. Then the deviatoric stress tensor **s** and the pressure p can be calculated for each phase, using constitutive parameters attached to this phase. This step is followed by an averaging of $\boldsymbol{s}$ and p, according to the linear mixing law:

$$\boldsymbol{s}=g_k\boldsymbol{s}_k \qquad p=g_k p_k \tag{10}$$

Modeling of Material Deposit

First of all, since the calculations are carried out in a Eulerian frame, the whole structure including the weld joint must be meshed. For that purpose, at the beginning of the simulation, a box, which will contain the final weld joint must be defined and meshed, as shown in Figure 2 (left). It is important to notice that the shape of the box will not drive the shape of the weld joint. Then, a geometrical object, C (a cone for instance) and its kinematics are defined. At each time step, elements of the mesh belonging to both the box boundary and the cone define the inlet surface for the filler metal. It is assumed here that during the material deposit, there is no formation of multiple droplets, but a continuous flow of filler material. Figure 2 (right) illustrates the main steps of the weld joint formation.

Figure 2. On the left, the meshes of the plate (in red) and of the box for weld bead formation (in blue). On the right, different steps of the weld joint formation.

The flow of the filler liquid metal is solved concurrently with the mechanical problem in the assembly. This is done through a VOF-like formulation in the reception box for the weld bead. In the elements of this box, a VOF (volume of fluid) function α is considered. Hence the deviatoric stress tensor $\boldsymbol{s}$ and the density ρ appearing in (9a) result from the following mixing law:

$$\begin{aligned}\boldsymbol{s}&=2\alpha\,\boldsymbol{s}_{metal}(\boldsymbol{v})+2(1-\alpha)\mu_{air}\dot{\boldsymbol{\varepsilon}}\\ \rho&=\alpha\rho_{metal}+(1-\alpha)\rho_{air}\end{aligned} \tag{11}$$

where $\boldsymbol{s}_{metal}(\boldsymbol{v})$ is obtained by a viscoplastic or an elastic-viscoplastic constitutive equation, according to the local temperature. The air is considered as a compressible Newtonian medium with viscosity μ_{air}. Accordingly, a mixture rule is applied to the mass conservation, extending equation (9b) to:

$$\forall p^* \quad \int_\Omega p^* \left[\alpha \left(\nabla \cdot \boldsymbol{v} + \frac{1}{\rho_{metal}} \frac{\mathrm{d}\rho_{metal}}{\mathrm{d}t} \right) + (1-\alpha)(\nabla \cdot \boldsymbol{v} + \chi_{air} p) \right] \mathrm{d}V = 0 \tag{12}$$

where χ_{air} is the (high) compressibility modulus in the air surrounding the filler material.
In order to track the interface between the flow of filler material and the air, an additional transport equation is solved for the VOF function α:

$$\frac{\partial \alpha}{\partial t} + \boldsymbol{v} \cdot \nabla \alpha = 0 \tag{13}$$

Figure 3 illustrates a material deposit on a plate without chamfer at different times during the process.

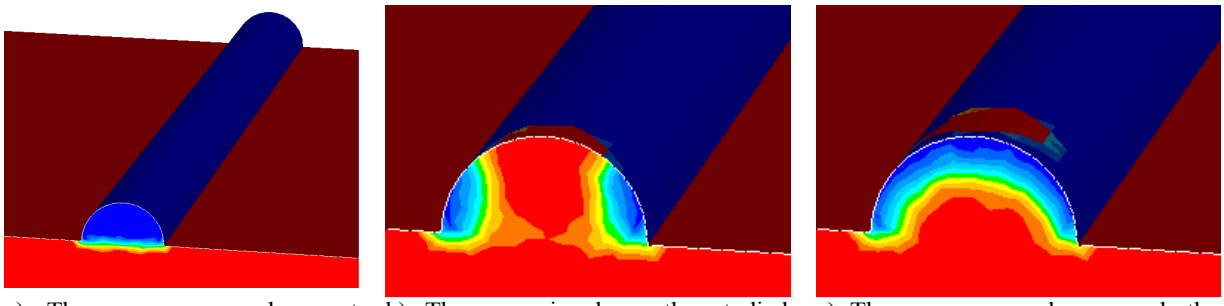

a) The source cone has not reached the studied section yet (in the foreground).

b) The cone is above the studied section: the filler material flows to form the weld bead.

c) The source cone has passed: the weld bead is no longer fed.

Figure 3. Formation of a weld bead on a plate.

Application and Validation: TIG Welding of Steel Plates

Among several application tests, we present here the one issued from the experimental work of Depradeux [11]. It consists of a TIG welding processed on a thick plate of 316L stainless steel, without filler material. Figure 4 shows the geometry and the tetrahedral mesh which is refined (1 mm) along the welding path, and rather coarse in the rest of the sheet (7 mm).

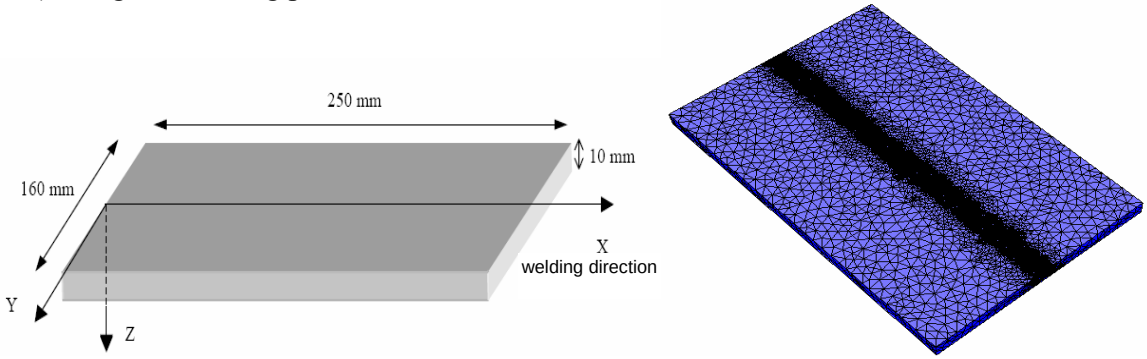

Figure 4. TIG welding on a thick plate: geometry and finite element mesh.

The aim of the test is to assess the ability of the numerical simulation to predict the transient temperature field. As specified in [11], the effective heat input is 13 MW/m^2, and it is assumed uniformly distributed in a 5 mm source radius. The welding speed is 1 mm/s. The temperature dependent thermophysical properties of the material and the radiative and convective thermal exchanges with the environment are taken as specified in [11]. However, the thermal conductivity is doubled for temperature exceeding the melting temperature, in order to simulate the temperature homogenization due to fluid flow in the weld pool [12]. Figure 5 and Figure 6 show the temperature evolution on the upper face of the plate at a lateral distance of 10 mm from

the weld line and on the lower face at lateral distances 0 mm (just under the line) and 10 mm. The results of the numerical model are in excellent agreement with the measurements.

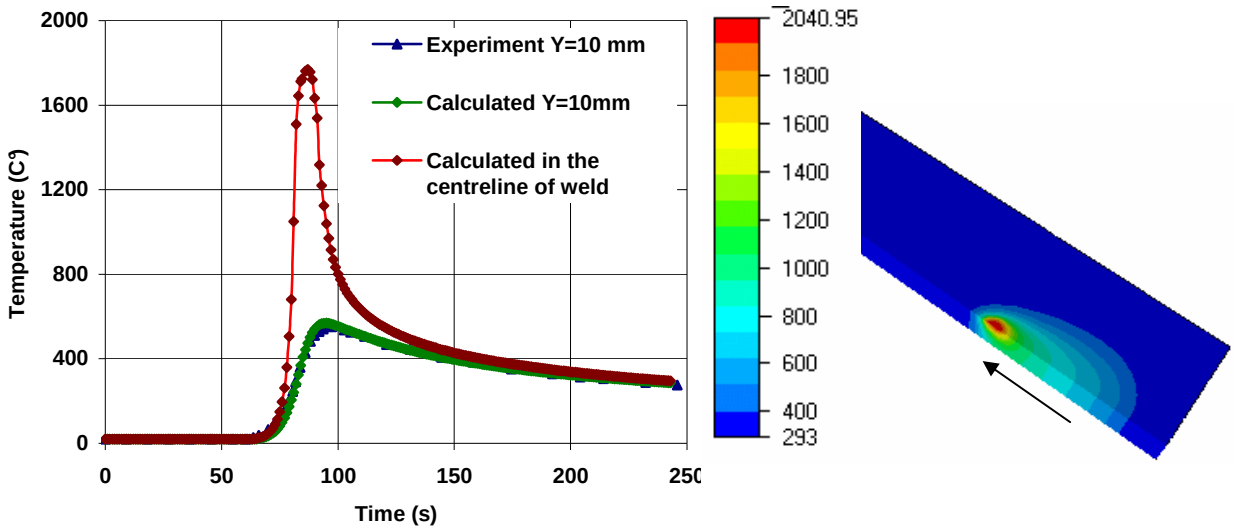

Figure 5. On the left: temperature evolution on the upper face of the plate at two locations: x = 95 mm, y = 10 mm (calculated and measured [11]) and x = 95 mm, y = 0 mm (calculated). On the right: temperature distribution on the upper face and vertical section.

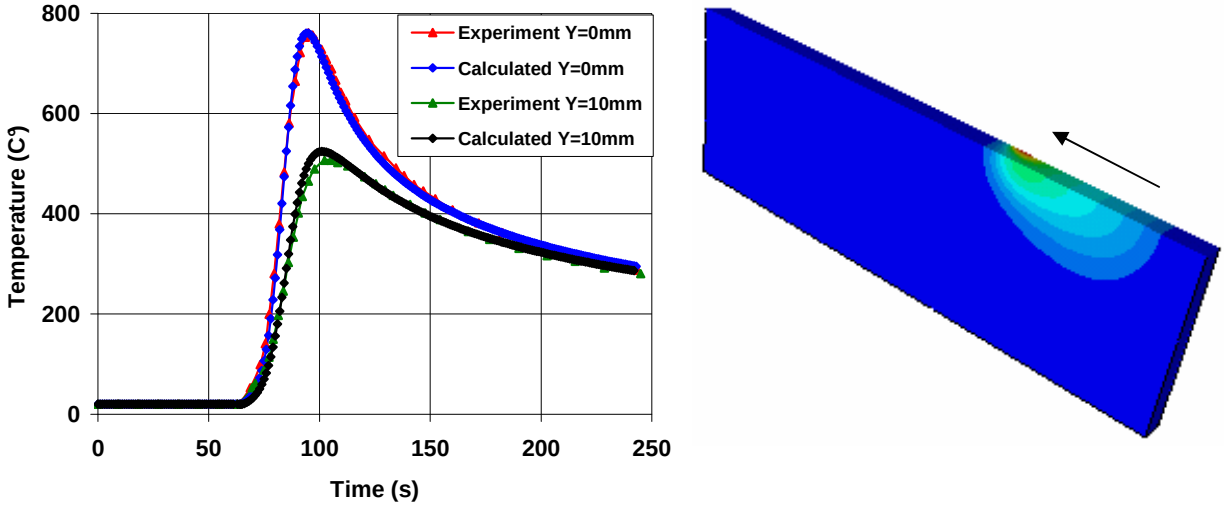

Figure 6. On the left: measured [11] and calculated temperature evolutions on the lower face of the plate at two locations (x = 95 mm, y = 0 and 10 mm). On the right: temperature distribution on the lower face and vertical section.

The comparison between the calculated weld pool and a picture of the melted zone, from the reference [11] shows again a very good agreement (Figure 7, left). It validates the heat source modeling for the test case with a weld speed of 1 mm/s. However, when taking a lower weld speed (0.67 mm/s), it can be seen in Figure 7 right that the weld pool depth is clearly underestimated in the numerical simulation, probably because the fluid convection in the weld pool is neglected in the present study. It can be thought that at lower weld speed, convection effects such as the Marangoni effect can fully develop and modify the transport of energy, and consequently the weld pool shape. In this case, a simple modification of the heat conductivity is not adequate: the solution consists then in identifying volume heat sources that could mimic such effects, or – better – in modeling concurrently the fluid flow in the pool, using a more refined finite element mesh which has to be dynamically adapted to follow the electrode trajectory.

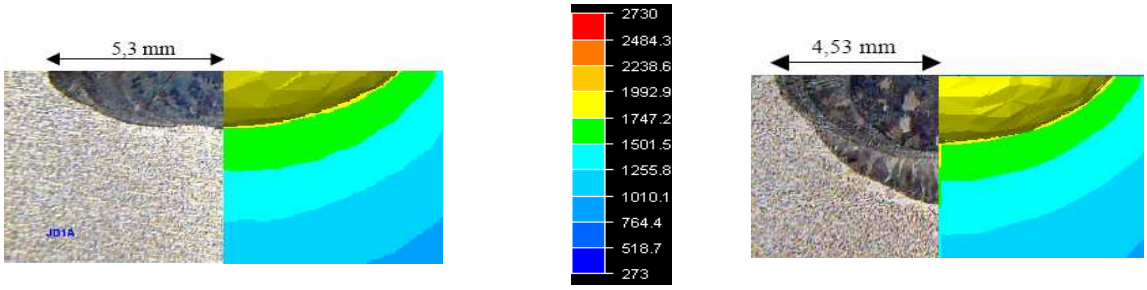

Figure 7. Comparison between observed [11] and calculated melted zones for two weld speeds.

The 316L steel being entirely austenitic from room temperature to its temperature of fusion, no metallurgical transformation occurs in the heat affected zone (HAZ). Therefore, in order to test and illustrate the metallurgical-thermal coupling, the same welding test has been simulated, but using the data of A508 steel. Austenization and solid state phase change have been considered according to the formulation described above. The bainite fraction reaches a maximum value of 85% and is shown in Figure 8a. The bainitic phase is surrounded in the HAZ by a thin layer of ferrite phase as shown in Figure 8d. The parent material of a welded plate outside the HAZ consists of the initial pearlite (60%) and ferrite (40%) as shown in Figure 8c and d.

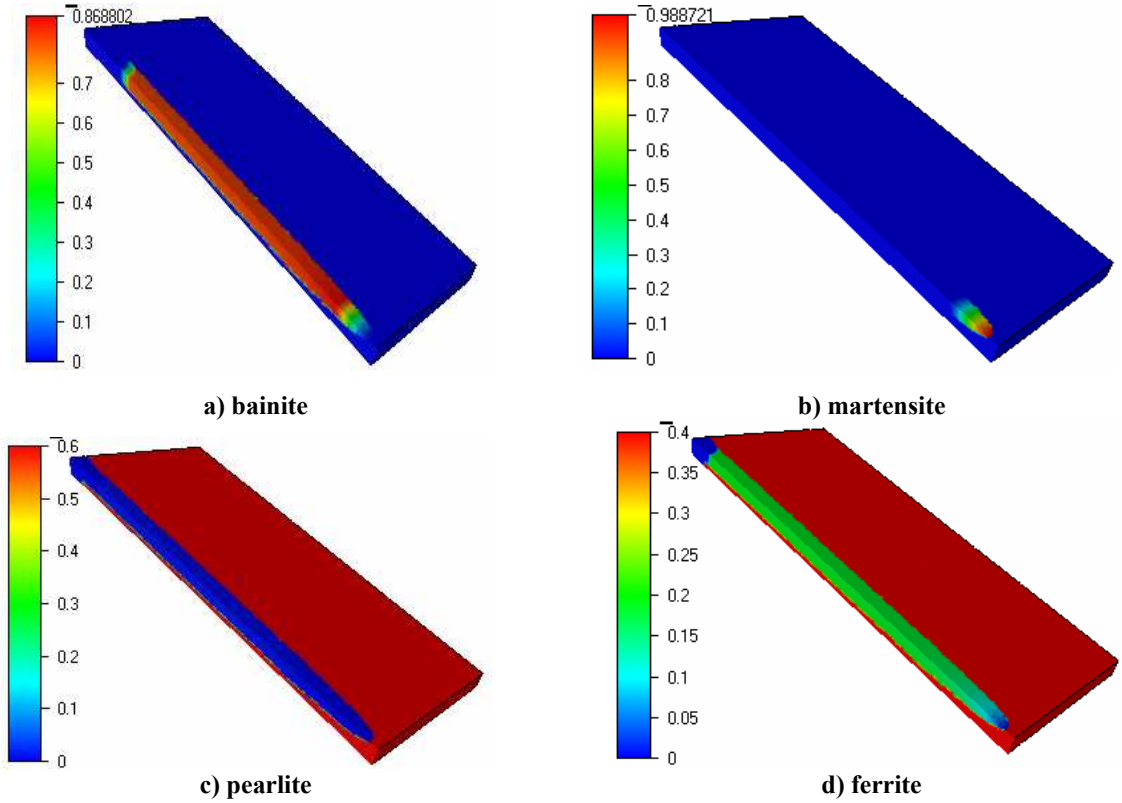

Figure 8. Calculated volume fractions of the different phases at the end of welding.

Figure 9 (left) shows the minor influence of phase changes on heat transfer by the release or transformation heat. In a first approach, a unique value of 76500 J/kg has been used for the transformations of austenite into ferrite, pearlite, bainite or martensite. The temperature evolution is slightly perturbed during cooling due to the bainitic transformation (110 s < t < 130 s). The transient microstructural changes at point (x = 95 mm, y = 0, z = 0) are given in Figure 9b, showing the rapid austenite formation (80 s < t < 81 s) and its decomposition, yielding in this case a bainitic-ferritic structure.

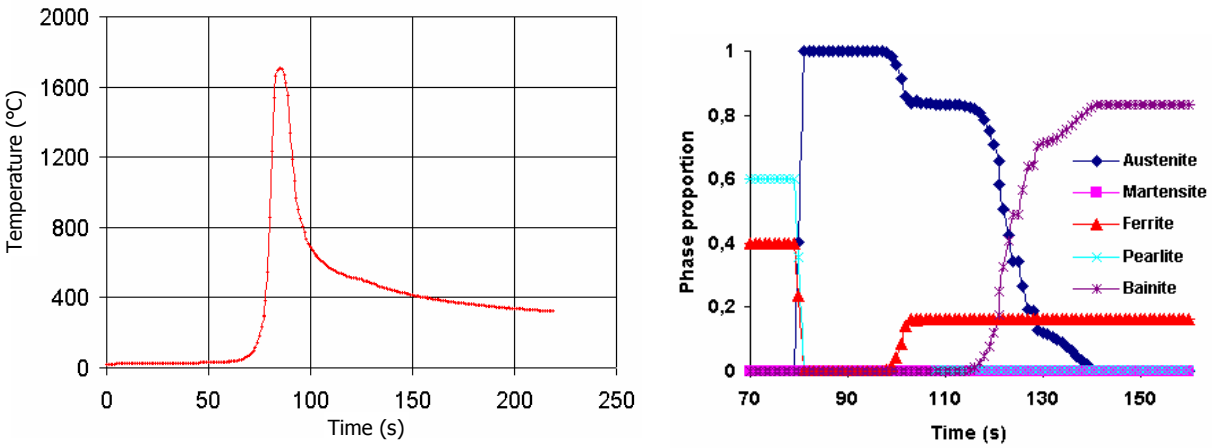

Figure 9. On the left: calculated temperature evolution on the upper face of the plate at location (x = 95 mm, y = 0). On the right: transient microstructural changes at the same location.

References

1. K. Runesson, A. Skyttebol, L.E. Lindgren, Nonlinear finite element analysis and application to welded structures, in Numer. and Comput. Meth., B. Karihaloo (ed.), Elsevier (2003) 255-320.
2. T. Inoue, D.Y. Ju, K. Arimoto, Metallo-thermo-mechanical simulation of quenching process, theory and implementation of computer code 'hearths', Proc. 1st Int. Conf. on Quenching and Control of Distortion, Chicago, USA (1992).
3. C. Aliaga, Simulation numérique par éléments finis 3D du comportement thermomécanique au cours du traitement thermique d'acier : application à la trempe de pièces forgées ou coulées, Ph.D. thesis (in French), Ecole Nationale Supérieure des Mines de Paris (2000).
4. W.A. Johnson, R.F. Mehl, Reaction kinetics in processes of nucleation and growth, Trans. Amer. Inst. Min. Eng. 135 (1939) 416-442.
5. F.M. Fernandes, S. Denis, A. Simon, Prévision de l'évolution thermique et structurale des aciers au cours de leur refroidissement continu, Mémoires et Etudes Scientifiques Revue de Métallurgie (in French) (1986) 355-366.
6. D.P. Koistinen, R.E. Marburger, A new kinetic model for anisothermal metallurgical transformation in pure Fe–C alloys and plain carbon steels, Acta Metall. 7 (1959) 59-60.
7. E. Gautier, J.S. Zhang, X.M. Zhang, Martensitic transformation under stress in ferrous alloys. Mechanical behaviour and resulting morphologies, Journal de Physique IV (1995) 451.
8. M. Rappaz, M. Bellet, M. Deville, Numerical Modeling in Materials Science and Engineering, Springer Series in Computational Mathematics, Springer-Verlag, 2003.
9. M. Bellet, C. Aliaga, O. Jaouen, Finite elements for a thermomechanical of analysis of solidification processes, Proc. MCWASP IX, 9th Int. Conf. on Modeling of Casting, Welding and Advanced Solidification Processes, Shaker Verlag, Aachen (2000) 10-17.
10. M. Bellet, O. Jaouen, I. Poitrault, An ALE-FEM Approach to the Thermomechanics of Solidification Processes with Application to the Prediction of Pipe Shrinkage, Int. J. Num. Meth. Heat Fluid Flow 15 (2005) 120-142.
11. L. Depradeux, Simulation numérique du soudage - acier 316L : validation sur cas tests de complexité croissante, Ph.D. thesis (in French), Institut National des Sciences Appliquées de Lyon (2004).
12. B. Brickstad, B.L. Josefson, A parametric study of residual stresses in multi-pass butt-welded stainless steel pipes, Int. J. Pressure Vessels and Piping 75 (1998) 11-25.

Acknowledgements

This study was supported by the companies Aubert et Duval and Industeel Creusot.